

The instability of Wilton ripples

Olga Trichtchenko^{*†}

Bernard Deconinck[‡]

Jon Wilkening[§]

June 4, 2016

Abstract

Wilton ripples are a type of periodic traveling wave solution of the full water wave problem incorporating the effects of surface tension. They are characterized by a resonance phenomenon that alters the order at which the resonant harmonic mode enters in a perturbation expansion. We compute such solutions using non-perturbative numerical methods and investigate their stability by examining the spectrum of the water wave problem linearized about the resonant traveling wave. Instabilities are observed that differ from any previously found in the context of the water wave problem.

Keywords

Wilton ripples, resonant gravity-capillary waves, high-frequency instabilities

Highlights

- Numerical solutions to Euler’s equations for periodic gravity-capillary waves
- A variant of the boundary integral method for traveling wave solutions is introduced
- Stability of Wilton ripple solutions to Euler’s equations is examined
- New instabilities are present due to the resonance condition being satisfied

1 Introduction

In 1915 J. R. Wilton [33] included the effects of surface tension and constructed a series expansion in terms of the amplitude of one-dimensional periodic waves in water of infinite depth, extending Stokes’s work [26]. He noticed that if the (non-dimensionalized) coefficient of surface tension equals $1/n$ ($n \in \mathbb{Z}^+$), the Stokes expansions giving traveling wave solutions to Euler’s equations are singular. As a way to rectify the problem, he modified the form of the perturbation expansion so that the n th harmonic enters at order $(n - 1)$ or $(n - 2)$ instead of n . The resulting solutions are known as resonant harmonics or Wilton ripples.

The occurrence of Wilton ripples is not merely a mathematical phenomenon. Henderson and Hammack [12] generated and observed such waves in a controlled tank experiment. In the experiment, several sensors were placed at different points along the length of the tank. They measured the wave profile and the frequencies of the wave as it travelled down the tank. Even though waves of roughly 20Hz were generated by the paddles at one end of the tank, frequencies around 10Hz were observed as well. This is a manifestation of Wilton ripples.

^{*}corresponding author

[†]Department of Mathematics, University College London, London, UK (o.trichtchenko@ucl.ac.uk)

[‡]Department of Applied Mathematics, University of Washington, Seattle, WA 98195-3925. (deconinc@uw.edu)

[§]Department of Mathematics, University of California, Berkeley, CA 94720-3840. (wilken@math.berkeley.edu)

McGoldrick contributed significantly to the understanding of gravity-capillary waves and their relation to resonant interaction, using both experiment and theory. He demonstrated experimentally that gravity-capillary waves lose their initial profile as they propagate [21]. He also examined these waves using weakly nonlinear theory [22] and used the method of multiple scales [23] to investigate the evolution of the gravity-capillary waves. Further, resonant phenomena such as Wilton ripples have been studied in model equations. For instance Boyd and Haupt [11] investigated Wilton ripples in the context of the so-called super Korteweg-de Vries or Kawahara [17] equation by adding resonant harmonics into the series expansion, following Wilton's original approach [26]. Akers and Gao [1] derived an explicit series solution for the Wilton ripples in this same context.

It is known that capillary-gravity waves exhibit a Benjamin-Feir instability [10], but not much work has been done analyzing the stability of Wilton ripples outside of that. In fact, we are aware only of the work of Jones [16, 15]. He investigated a system of coupled partial differential equations describing up to cubic order the interaction of the fundamental mode of a gravity-capillary wave with its second harmonic. He also provided wave train solutions of these equations. These were used to examine the stability of gravity-capillary waves as different parameters are varied. We will analyze the stability of resonant solutions by looking at the stability eigenvalue problem obtained by linearizing around a steady state solution. This was previously done by McLean [24] who built on numerical work of Longuet-Higgins [18, 19] as well as others to examine growth rates of instabilities as a function of wave steepness. We will also use the ideas seen in MacKay and Saffman [20] and use the Hamiltonian structure of the problem in order to find where instabilities can occur.

In this paper, working with fully nonlinear solutions of the water wave equations, we investigate the spectral stability of resonant gravity-capillary waves using the Fourier-Floquet-Hill method [7]. To our knowledge, our work presents the first study of the different instabilities to which Wilton ripples are susceptible, without restricting the nature of the disturbances. Our paper follows the previous investigations on the instabilities of one-dimensional periodic traveling gravity waves [8] and of gravity waves in the presence of weak surface tension [9]. More details and a more comprehensive investigation of the different types of solutions, their series expansions, and their instabilities will be published elsewhere [27].

2 Computing Resonant Gravity-Capillary Waves

One-dimensional gravity-capillary waves are governed by the Euler equations,

$$\phi_{xx} + \phi_{zz} = 0, \quad (x, z) \in D, \quad (1a)$$

$$\phi_z = 0, \quad z = -h, \quad x \in (0, L), \quad (1b)$$

$$\eta_t + \eta_x \phi_x = \phi_z, \quad z = \eta(x, t), \quad x \in (0, L), \quad (1c)$$

$$\phi_t + \frac{1}{2} (\phi_x^2 + \phi_z^2) + g\eta = \sigma \frac{\eta_{xx}}{(1 + \eta_x^2)^{3/2}}, \quad z = \eta(x, t), \quad x \in (0, L), \quad (1d)$$

which incorporate the effects of both gravity and surface tension, where g is the acceleration due to gravity and σ is the coefficient of surface tension. Here h is the height of the fluid when at rest, $\eta(x, t)$ is the elevation of the fluid surface and $\phi(x, z, t)$ is the velocity potential. As was shown in [29], we can add an arbitrary function $C_\phi(t)$ (of time but not space) to the Bernoulli condition (1d), which we will do for computational purposes below. We focus on solutions on a periodic domain $D = \{(x, z) \mid 0 \leq x < L, -h < z < \eta(x, t)\}$ as shown in Figure 1. It is clear that the parameter space for the traveling-wave solutions of this problem is extensive. A comprehensive investigation will be presented in [27]. In this brief communication, we restrict our attention to solutions for which $g = 1$, the period $L = 2\pi$ and the water depth $h = 0.05$. If one employs the criteria of [2, 3, 30], this puts us in the shallow water regime, quite different from Wilton [33] who worked with $h = \infty$. However, it should be noted that the above references distinguishing shallow water from deep water do not incorporate surface tension, and as such their results do not immediately apply.

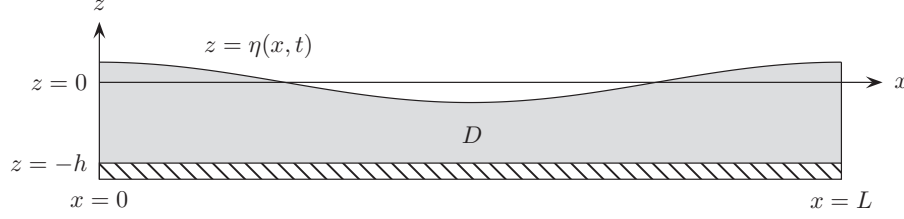


Figure 1: The domain on which we solve Euler's equations.

The regular perturbation expansion (or Stokes expansion) for a 2π -periodic traveling water wave takes the form

$$\eta(x) = \epsilon \cos x + \sum_{k=2}^{\infty} \epsilon^k \eta_k(x), \quad \eta_k(x) = \sum_{j=2}^k 2\hat{\eta}_{kj} \cos(jx), \quad (2)$$

where the Euler equations are reduced using the traveling wave reduction $\partial_t \rightarrow -c\partial_x$. Regular perturbation theory (see, for instance, [28]) leads to an expression for $\eta_k(x)$ with a denominator proportional to the left-hand side of

$$(g + \sigma)k \tanh(h) - (g + k^2\sigma) \tanh(kh) = 0, \quad (k \neq 1). \quad (3)$$

We refer to (3) as the resonance condition as it indicates that the k -th harmonic is resonant with the base mode. If resonance occurs, *i.e.* (3) holds for a certain value of k , say $k = K$, the regular Stokes expansion breaks down, and it is not possible to determine $\eta_K(x)$ in the form (2). Instead, the resonant harmonic arises in the Stokes series at order ϵ^{K-1} or ϵ^{K-2} [28, 33]. It is easy to see that (3) cannot hold when $\sigma = 0$. In other words, surface tension is a necessary condition for the occurrence of resonance. Further, (3) holds for at most one value of $k \geq 2$; see Appendix A. Throughout this paper, we fix the surface tension parameter consistently so that resonance occurs for $k = 10$ ($\sigma \approx 8.20 \times 10^{-4}$). This is an arbitrary choice, of course, and other choices can be made.

To compute traveling solutions of (1a-d), we developed a variant of the boundary integral method of Wilkening & Yu for the time-periodic problem [32], modified to take advantage of the traveling wave assumption. Considering only the equations (1c-d), which are valid at the surface $z = \eta$, and defining a surface velocity potential $q(x, t) = \phi(x, \eta(x, t), t)$, we have

$$-c\eta_x = \phi_z - \eta_x \phi_x := G(\eta)q, \quad (4a)$$

$$-cq_x = P \left[-c\phi_z \eta_x - \frac{1}{2} (\phi_x^2 + \phi_z^2) - g\eta + \sigma \frac{\eta_{xx}}{(1 + \eta_x^2)^{3/2}} \right]. \quad (4b)$$

Here (4b) is obtained from (1d) by using $q_t = \phi_t + \phi_z \eta_t$ at the free surface prior to restricting to a traveling frame. Equation (4a) defines the Dirichlet to Neumann operator $G(\eta)$. Further, P is the projection operator onto functions of zero mean: $Pf(x) = f(x) - \frac{1}{2\pi} \int_0^{2\pi} f(x) dx$. The introduction of this operator is required since the left-hand side of (4b) clearly has zero average. This amounts to including $C_\phi(t)$ in (1d) to avoid secular growth in $\phi(t)$ as the wave travels. In addition, in the next step we invert $G(\eta)$. Working with functions of zero average guarantees the existence of a unique inverse.

As written, (4a-b) is a system of two equations for the two unknown surface variables $q(x)$ and $\eta(x)$, linked by $\phi(x, z)$ through the solution of Laplace's equation (1a) in the domain D . We solve the first equation for $q(x)$ using the inverse $G(\eta)^{-1}$ of the Dirichlet to Neumann operator [5]:

$$q = -cG(\eta)^{-1}\eta_x, \quad \begin{pmatrix} \phi_x \\ \phi_z \end{pmatrix} = \frac{1}{1 + \eta_x^2} \begin{pmatrix} 1 & -\eta_x \\ \eta_x & 1 \end{pmatrix} \begin{pmatrix} q_x \\ -c\eta_x \end{pmatrix}. \quad (5)$$

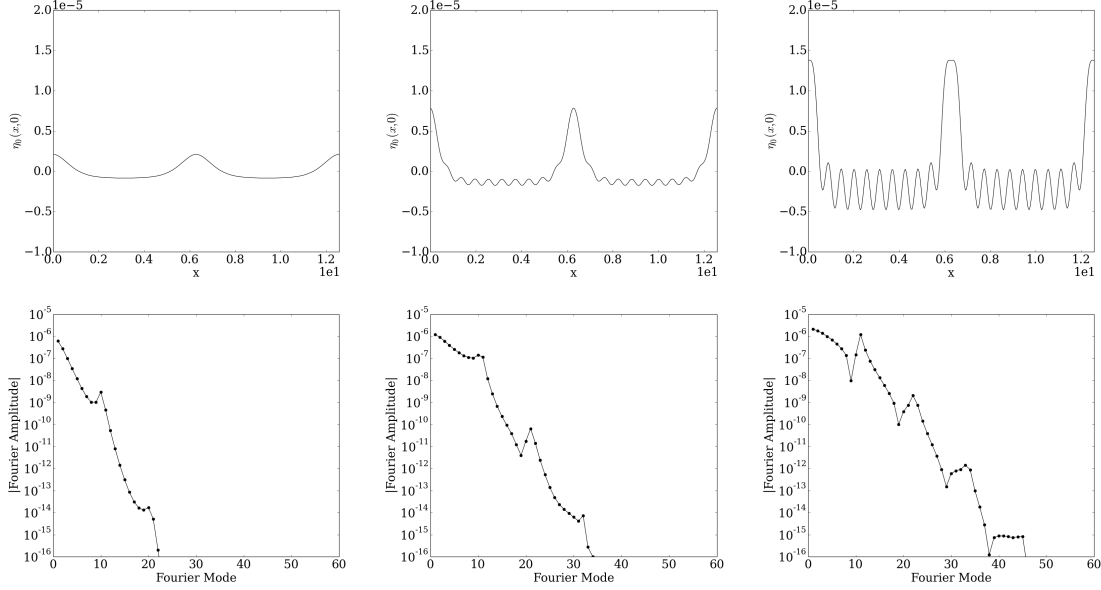


Figure 2: Wave profiles for solutions with amplitude $\epsilon = 2\hat{\eta}_1 = 1.244 \times 10^{-6}$, 2.448×10^{-6} and 4.254×10^{-6} (top), and semi-log plots of the absolute values of their Fourier modes $\hat{\eta}_k$ (bottom). Here $\hat{\eta}_k = \frac{1}{2\pi} \int_0^{2\pi} \eta(x) e^{-ikx} dx$. As expected from the results for gravity waves [8], the troughs get wider and the crests become more narrow as the amplitude increases. The resonant harmonic also becomes more apparent, especially in the troughs. For the wave of highest amplitude plotted, a depression is present in the crest.

This determines q , ϕ_x and ϕ_z on the free surface given η . Equation (4b) may then be rewritten as $R(c, \eta) = 0$, with

$$R(c, \eta) := P \left[c\phi_x - \frac{1}{2}\phi_x^2 - \frac{1}{2}\phi_z^2 - g\eta + \sigma\partial_x \left(\frac{\eta_x}{(1 + \eta_x^2)^{1/2}} \right) \right], \quad (6)$$

where we moved cq_x inside $P[\dots]$ and used $q_x = \phi_x + \phi_z\eta_x$. Next we define the objective function $F(c, \eta) = \frac{1}{4\pi} \int_0^{2\pi} R(c, \eta)^2 dx$, which is minimized (holding the first Fourier mode of η fixed at the desired amplitude, $\hat{\eta}_1 = \epsilon/2$) using the modified Levenberg-Marquardt method developed by Wilkening and Yu in [32].

Rather than computing the operator $G(\eta)$ as described in [32] and inverting it in (5), we reverse the algorithm to directly compute the Neumann to Dirichlet operator. In more detail, $G(\eta)q$ can be computed by first solving a second-kind Fredholm integral equation $[\frac{1}{2}\mathbb{I} + \mathbb{K}]\mu = q$ to find the dipole density μ , and then evaluating $G(\eta)q = [\frac{1}{2}H + \mathbb{G}]\mu'$, where H is the Hilbert transform. Formulas for \mathbb{K} and \mathbb{G} are given in [32]. The modification is to solve $[\frac{1}{2}H + \mathbb{G}]\mu' = -c\eta_x$ for μ' , which is essentially a second-kind Fredholm integral equation due to $H^2 = -P$; take an antiderivative to find μ ; and evaluate $q = [\frac{1}{2}\mathbb{I} + \mathbb{K}]\mu$. The improved accuracy comes from taking an antiderivative instead of a derivative in the middle step. A similar idea was used by Sethian and Wilkening [25] in the context of linear elasticity to avoid loss of digits when evolving a semigroup whose generator involves two spatial derivatives of a type of Dirichlet-Neumann operator — the inverse operator can be computed much more accurately.

Figure 2 displays laptop-computed solutions running compiled C++ code implementing the method sketched above. We use as many Fourier modes as needed to ensure the highest modes decay to double or quadruple-precision roundoff thresholds. A key difference between these numerical results and those for gravity waves with a small coefficient of surface tension [9] is that the Fourier modes

no longer decay monotonically. The solutions computed here show a resonance at the $K = 10$ th mode and its higher harmonics. As the amplitude is increased, the modes neighboring the resonant modes start to grow as well.

3 Stability

We examine the stability of the solutions of the previous section using the Fourier-Floquet-Hill numerical method described in [7]. Convergence theorems for this method are found in [6, 14]. Denoting one of the traveling solutions computed above by $(\eta_0; q_0)$, we consider a perturbed solution

$$\eta(x, t) = \eta_0(x - ct) + \delta\eta_1(x - ct)e^{\lambda t} + \dots, \quad q(x, t) = q_0(x - ct) + \delta q_1(x - ct)e^{\lambda t} + \dots \quad (7)$$

Here $(\eta_1; q_1)$ is the spatial part of the perturbation, bounded for all x , including as $|x| \rightarrow \infty$. Specifically, $\eta_1(x)$ is not required to be periodic with the same period as $\eta_0(x)$. Note that $\text{Re}(\lambda) > 0$ implies exponential growth of the perturbed solution, and thus instability of $\eta_0(x)$. Substitution of (7) in the governing equations (1a-d) and neglecting terms of order δ^2 yields a linear (but nonlocal) generalized eigenvalue problem for η_1, q_1 that is invariant under spatial translation by 2π ; see [8, 9]. Therefore we expect η_1, q_1 to also be eigenfunctions of the shift operator, and hence be of Bloch form

$$\begin{pmatrix} \eta_1(x) \\ q_1(x) \end{pmatrix} = e^{i\mu x} \sum_{m=-\infty}^{\infty} \begin{pmatrix} \hat{N}_m \\ \hat{Q}_m \end{pmatrix} e^{imx} = \sum_{m=-\infty}^{\infty} \begin{pmatrix} \hat{N}_m \\ \hat{Q}_m \end{pmatrix} e^{i(m+\mu)x}, \quad \mu \in (-1/2, 1/2]. \quad (8)$$

Due to the Hamiltonian nature of (1a-d) [34], the spectrum of this generalized eigenvalue problem is reflection symmetric with respect to both the real and imaginary axes [31]. As a consequence, the presence of any eigenvalue λ off the imaginary axis implies instability.

For the case of flat water ($\eta_0(x) \equiv 0$), the spectrum may be computed analytically. It consists of all values of the form

$$\lambda_{\mu+m}^{\pm} = ic(\mu + m) \pm i\sqrt{[g(\mu + m) + \sigma(\mu + m)^3] \tanh((\mu + m)h)}, \quad \mu \in (-1/2, 1/2], \quad m \in \mathbb{Z}, \quad (9)$$

where $c = \sqrt{(g + \sigma) \tanh h}$ is the wave speed in the linearized regime. Since these values are all imaginary, we conclude that flat water is spectrally stable. However, as we examine solutions with a nonzero amplitude, instabilities arise. Figures 3 and 4 show detailed stability results for the three larger-amplitude solutions of Figure 2. Figure 3 shows the complex λ plane, while Figure 4 shows $\text{Re}(\lambda)$ vs μ . Many phenomena are similar to those observed for gravity [8] and (non-resonant) gravity-capillary [9] waves, such as the presence of bubbles of high-frequency instabilities for the larger-amplitude waves. New phenomena are observed as well. We observe nested structures for the two larger-amplitude waves, and, despite being in shallow water, we notice the presence of a modulational instability (columns 2 and 3). As shown in the right panel of Figure 5, the onset of this modulational instability occurs around $\epsilon = 1.555 \times 10^{-6}$, when the large bubble of instability present at that amplitude merges with its mirror image at the origin.

Since eigenvalues are continuous with respect to variations of the wave amplitude [13], eigenvalues may leave the imaginary axis as the amplitude increases only through collisions on the imaginary axis. This is required to ensure the Hamiltonian symmetry of the spectrum. Thus, a necessary condition for the loss of stability of $\eta_0(x)$ as the solution bifurcates away from the flat water state is that there exist μ and m such that one of the following conditions holds:

$$\lambda_{\mu}^{+} = \lambda_{\mu+m}^{+}, \quad \lambda_{\mu}^{+} = \lambda_{\mu+m}^{-}, \quad \lambda_{\mu}^{-} = \lambda_{\mu+m}^{+}, \quad \lambda_{\mu}^{-} = \lambda_{\mu+m}^{-}. \quad (10)$$

For the resonant solutions with $K = 10$, we have a six-way crossing at $\lambda = 0$ when $\mu = 0$, namely

$$\lambda_{\mu}^{+} = \lambda_{\mu}^{-} = \lambda_{\mu-1}^{+} = \lambda_{\mu+1}^{-} = \lambda_{\mu-10}^{+} = \lambda_{\mu+10}^{-} = 0, \quad (\mu = 0). \quad (11)$$

To show that $\lambda_{\mu-10}^{+} = 0$ and $\lambda_{\mu+10}^{-} = 0$, the resonance condition (3) may be used in (9). As shown in Figure 5, two bubbles of instability nucleate at this six-way crossing. As the wave amplitude

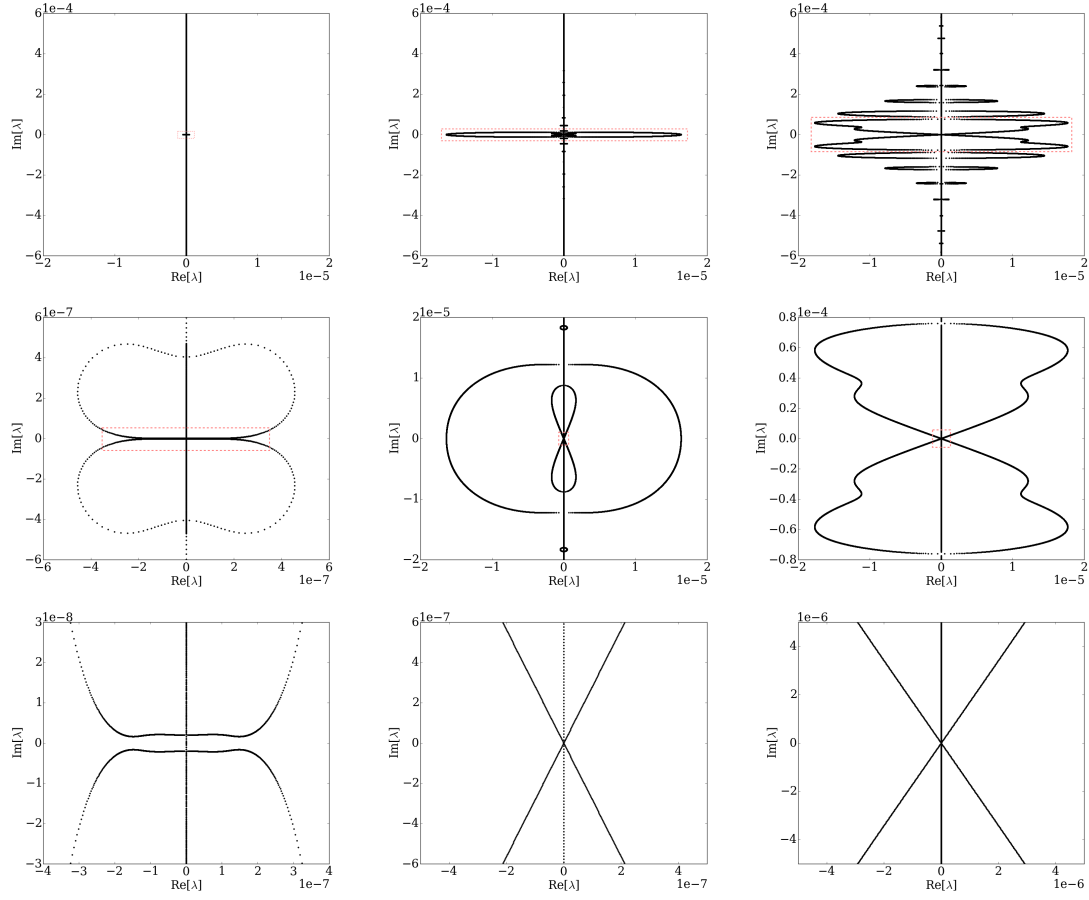


Figure 3: Stability results for the solutions shown in Figure 2. The columns correspond to $\epsilon = 1.244 \times 10^{-6}$, 2.448×10^{-6} , and 4.254×10^{-6} , respectively. For each amplitude, regions highlighted by the red box are magnified further and shown in the second and third rows. In the second and third column, the curves pass through the origin.

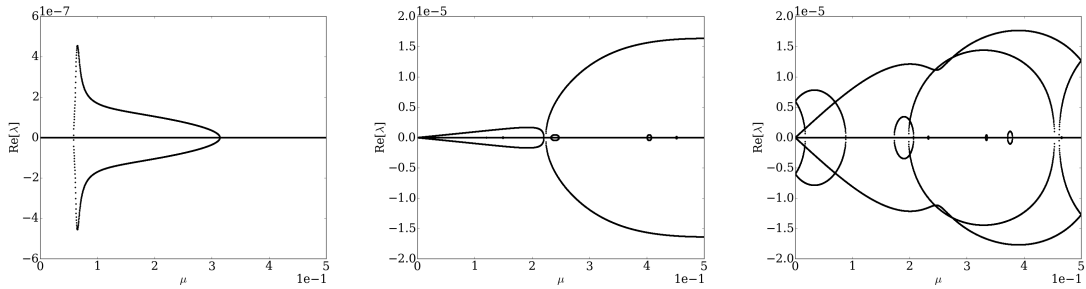


Figure 4: Dependence of $\text{Re}(\lambda)$ on μ for $\epsilon = 1.244 \times 10^{-6}$, 2.448×10^{-6} , and 4.254×10^{-6} .

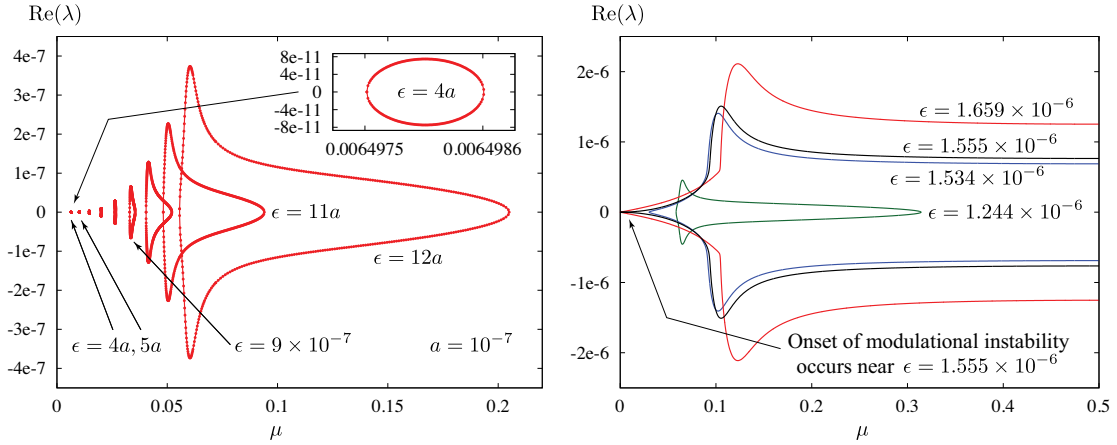


Figure 5: (left) Two bubbles of instability nucleate from the origin and move away from the $\text{Re}(\lambda)$ axis in opposite directions as ϵ increases from 0. The second bubble (with $\mu < 0$) is not shown as the figure is reflection symmetric about $\mu = 0$ (and also about $\mu = 1/2$, by periodicity). (right) At larger amplitudes, the bubble merges with its mirror image to the right, and later with its image to the left, at the origin.

ϵ increases away from zero, these instability bubbles leave the origin in the $\text{Re}(\lambda)$ vs μ plane in opposite directions, one to the right (shown in Fig. 5), and the other to the left, a mirror image of the one to the right. For small values of ϵ , the bubbles are supported on intervals well separated from the origin. Indeed, the range of values μ over which we observe an eigenvalue λ with $\text{Re}(\lambda) \neq 0$ has the form $(-\mu_{1,\epsilon}, -\mu_{0,\epsilon}) \cup (\mu_{0,\epsilon}, \mu_{1,\epsilon})$, with $0 < \mu_{0,\epsilon} < \mu_{1,\epsilon} < 1/2$. Although $\mu_{0,\epsilon}$ and $\mu_{1,\epsilon}$ both approach zero as $\epsilon \rightarrow 0^+$, the width $\mu_{1,\epsilon} - \mu_{0,\epsilon}$ of each interval is much smaller than the gap $2\mu_{0,\epsilon}$ between intervals. For example, in the inset of the left panel of Fig. 5, when $\epsilon = 4 \times 10^{-7}$, the width is 1.09×10^{-6} while the gap is 11900 times larger. Thus, even though the instability nucleates at $\mu = 0$, it is not modulational since the wave numbers of the unstable perturbations are tightly confined to a narrow interval separated from the origin. In the right panel of Fig. 5, we see that as ϵ increases, the bubble grows in size, merges with its reflection about $\mu = 1/2$, and eventually forms a protrusion that connects with its reflection about $\mu = 0$ at the origin (around $\epsilon = 1.555 \times 10^{-6}$). Beyond this point, modulational instabilities are present.

We finish these preliminary stability considerations by examining the short-time effect of these instabilities on the water wave profiles they perturb. Given an eigenvalue-eigenfunction pair, the short-time dynamics of the perturbed wave profile is dictated by the linearized problem obtained above. We have

$$\eta(x + ct, t) \approx \eta_0(x) + \delta \text{Re}\{e^{i\theta} e^{\lambda t} \eta_1(x)\}, \quad \eta_1(x) = \sum_{m=-M}^M \hat{N}_m e^{i(m+\mu)x}, \quad (12)$$

where M is the number of Fourier modes of the computed eigenfunction and $\theta \in (-\pi, \pi]$ is an arbitrary phase; see [7, 8]. Since the eigenfunction corresponding to $\bar{\lambda}$ (associated with $-\mu$) is the complex conjugate of $\eta_1(x)$, $\text{Re}(e^{\lambda t} \eta_1(x))$ and $\text{Re}(e^{i\theta} e^{\lambda t} \eta_1(x))$ span the same space as $e^{\lambda t} \eta_1(x)$ and $e^{\lambda t} \bar{\eta}_1(x)$. If $\text{Re}(\lambda) \neq 0$, Hamiltonian symmetry implies that $-\lambda$ and $-\bar{\lambda}$ are also eigenvalues, and the eigenfunctions can be obtained by reversing the sign of q (i.e. reversing time) and reflecting space. However, we focus here on linearized solutions that grow as $t \rightarrow +\infty$ rather than decay. The eigenfunctions (η_1, q_1) are normalized so that $\sum_{|m| \leq N} |\hat{N}_m|^2 = 1$, with complex phase chosen so that \hat{N}_0 is real and positive. The Fourier modes of the eigenfunctions are found to decay exponentially, so it is not difficult to resolve a given eigenfunction to double-precision accuracy.

Figure 6 shows the results of seeding the traveling solution $\eta_0(x - ct)$ of amplitude $\epsilon = 1.244 \times 10^{-6}$

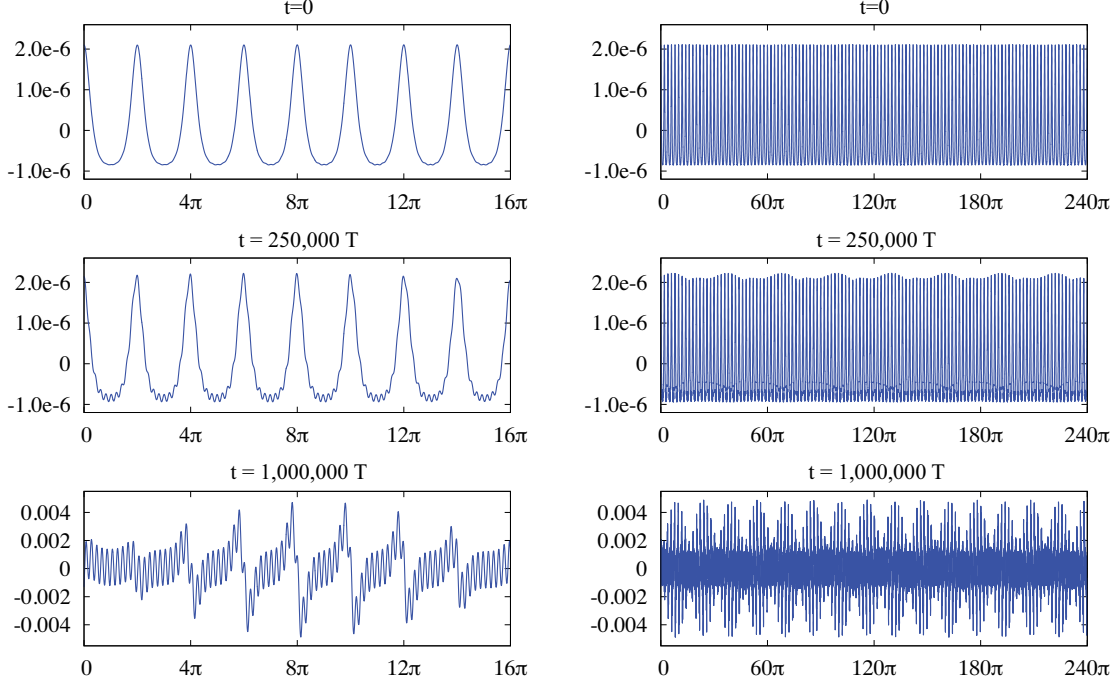


Figure 6: Three snapshots of a perturbation of the wave in the left column of Figure 2 (with amplitude $\epsilon = 1.244 \times 10^{-6}$), approximated by (12) and plotted over 8 (left) or 120 (right) periods of the wave. Here $\mu = 0.06496517$ corresponds to the most unstable eigenvalue, namely $\lambda = (4.557154 + 2.322777i) \times 10^{-7}$, and $T = 28.096$ is the time it takes the underlying traveling wave to traverse its wavelength. The unperturbed solution is in the resonant regime, but with secondary oscillations indiscernible at this amplitude.

with a multiple of the most unstable eigenfunction and using Equation 12. This traveling wave corresponds to the left panels of Figures 2, 3 and 4. From the results of Figure 4, $\text{Re}(\lambda)$ is maximized at $\mu = 0.06496417$ by $\lambda = (4.557154 + 2.322777i) \times 10^{-7}$. This maximal growth rate $\text{Re}(\lambda)$ is small in comparison to $1/T$, where the period $T = 2\pi/c = 28.09599$ is the time required for the underlying traveling wave to traverse its wavelength. Indeed, the perturbation is only amplified by $e^{\text{Re}(\lambda)T} = 1.0000128$ per cycle of the underlying wave. In Figure 6, the approximation (12) was used with $\theta = 0$ and $\delta = \epsilon/200$. With the above normalization $\sum_m |\hat{N}_m|^2 = 1$, we have

$$\|\eta_1\|_\infty = \max_{0 \leq x \leq 2\pi} |\eta_1(x)| = 2.159, \quad \|\delta\eta_1\|_\infty / \|\eta_0\|_\infty = 0.00639. \quad (13)$$

The left column of Figure 6 shows eight periods of the traveling wave while the right column shows 120 periods. In both columns, $\eta(x + ct, t)$ is plotted, showing the results in a frame traveling with the unperturbed wave. The rows show the perturbed solution at $t = 0$, $t = 250,000T$ and $t = 1,000,000T$, where $T = 2\pi/c = 28.09599$ is the time required for $\eta_0(x - ct)$ to traverse its wavelength. The effect of the initial perturbation is difficult to discern from η_0 in the top row of Figure 6. At $t = 250,000T$, the perturbation has grown large enough to be visible in the figure, yielding small ripples in the troughs and regular subharmonic variation in the heights of the wave crests. The third row ($t = 1,000,000T$) shows the long-time evolution using the linear problem. Unlike the second row, these graphs do not provide a good approximation of the nonlinear dynamics of the water wave surface. Rather, since the perturbation has grown to several orders of magnitude larger than the profile $\eta_0(x)$, the third panel in effect shows the eigenfunction profile.

These results show that with $\epsilon = 1.244 \times 10^{-6}$, which already deviates substantially from a sinusoidal wave profile (recall Fig. 2), the seeded wave can travel hundreds of thousands of wavelengths before losing coherence. Since $\text{Re}(\lambda)$ decreases rapidly as $\epsilon \rightarrow 0$ (recall Fig. 5), this effect

is even more pronounced at smaller amplitude. The two larger-amplitude waves studied in detail in Figures 2, 3 and 4 are more unstable, with multiple unstable branches of eigenvalue curves and larger values of $\text{Re}(\lambda)$, though still small compared to $1/T$.

4 Conclusion

Using numerical techniques similar to those in [8] and [9], as well as those introduced in [32], we compute periodic traveling wave solutions of the full water wave problem (1a-d) including the effects of surface tension. We focus specifically on solutions whose small-amplitude limits are fully resonant, the so-called Wilton ripples. We present the first computation of the stability spectra of these solutions, providing an overview of the different types of instabilities to which they are susceptible. The resonance condition allows for a collision of six eigenvalues, which leads to the nucleation of two bubbles of instability at positive wave amplitude ε . This instability mechanism does not occur in non-resonant gravity-capillary waves. Although these waves are mathematically unstable, the growth rates of these instabilities remain remarkably small, e.g. compared to the inverse of the period of the traveling wave, even for waves with amplitude well outside of the linear regime. For example, in Figure 6, we see that after seeding the nonlinear wave shown in the left column of Figure 2 with a perturbation in the most unstable direction with amplitude about 0.64% of that of the underlying wave, as in (12) and (13), the wave still travels hundreds of thousands of wavelengths before losing coherence. The growth rates of the instabilities are even smaller for smaller-amplitude waves, as shown in the left panel of Figure 5. For larger-amplitude resonant waves, new types of instabilities are observed, manifested as nested structures and Benjamin-Feir-like instabilities present in shallow water waves. More comprehensive studies of these solutions and their instabilities will be presented in [27]. These types of resonances appear in a more general context than the water waves [4] and understanding their behaviour in this context allows more insight into other resonant Hamiltonian systems.

5 Acknowledgements

This work was supported in part by the National Science Foundation through grant NSF-DMS-1008001 (BD), by the EPSRC under grant EP/J019569/1 and by NSERC (OT), and by the Director, Office of Science, Computational and Technology Research, U.S. Department of Energy under contract number DE-AC02-05CH11231 (JW). Any opinions, findings, and conclusions or recommendations expressed in this material are those of the authors and do not necessarily reflect the views of the funding sources.

A Uniqueness and the Resonance Condition

In this appendix, we show that there is at most one value $k > 1$ for which (3) holds, and we identify the parameter values for which resonance can occur. Let

$$f(x) = (1 + Ax^2) \frac{\tanh x}{x}, \quad A = \frac{\sigma}{gh^2}, \quad x > 0. \quad (14)$$

The resonance condition (3) is equivalent to $f(h) = f(kh)$, where $h > 0$ and $k > 1$. We ignore the requirement that k is an integer in what follows. See Figure 7 for plots of $f(x)$ for different values of A . If $A = 0$, then $f(x)$ decreases monotonically to 0 as $x \rightarrow \infty$, and the resonance condition does not hold. If $A > 0$, then $f(x) \rightarrow \infty$ as $x \rightarrow \infty$. If $A \geq 1/3$, we will show that $f(x)$ increases monotonically on $0 \leq x < \infty$, so the resonance condition does not hold. And if $0 < A < 1/3$, we claim that $f(x)$ decreases monotonically over an interval $[0, x_*]$, then increases monotonically without bound on $[x_*, \infty)$. The intermediate value theorem then implies that for $0 < h < x_*$, there exists $kh > x_*$ such that $f(kh) = f(h)$. If this value of k is an integer, resonance occurs; k is unique since f varies monotonically on either side of x^* .

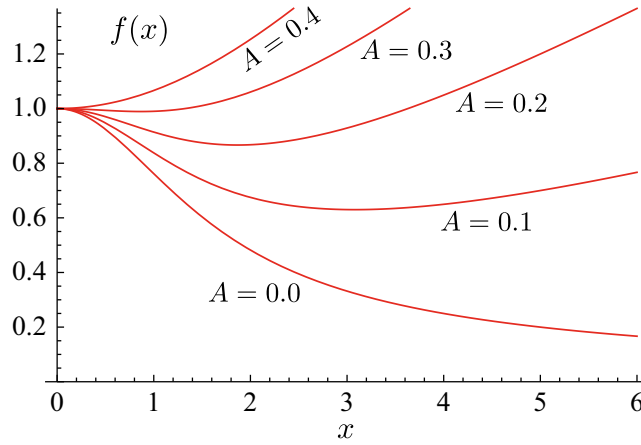


Figure 7: The graph of $f(x)$ in (14) for various values of A .

To complete the proof, we need to identify the sign of $f'(x)$ when $A > 0$ and $x > 0$. From

$$f'(x) = (-x^{-2} + A) \tanh x + (x^{-1} + Ax) \operatorname{sech}^2 x,$$

we have that the sign of $f'(x)$ is the same as the sign of $(\frac{2x}{\sinh 2x} - \frac{1-Ax^2}{1+Ax^2})$. In particular, $f'(x) > 0$ for $x \geq A^{-1/2}$. Let $x = A^{-1/2}y$. Then for $0 < y < 1$, $f'(x)$ has the same sign as

$$g(y) := \frac{1+y^2}{1-y^2} - \frac{\sinh(2y/\sqrt{A})}{2y/\sqrt{A}} = \sum_{n=1}^{\infty} (2-b_n)y^{2n}, \quad b_n = \frac{4^n}{A^n(2n+1)!}. \quad (15)$$

We note that $b_n = b_{n-1}c_n$ with $c_n = 4/[2n(2n+1)A]$. If $A \geq 1/3$ then $b_1 \leq 2$ and $b_n < b_{n-1} \leq 2$ for $n \geq 2$. It follows that $g(y) > 0$; hence, $f'(x) > 0$ for $x > 0$. If $A < 1/3$, then $b_1 > 2$ and $g(y) < 0$ for sufficiently small y . Since $c_n \rightarrow 0$ monotonically, there is an integer $N \geq 2$ such that $b_n > 2$ for $1 \leq n < N$; $b_N \leq 2$; and $b_n < 2$ for $n > N$. Since $g(1^-) = \infty$, there is a zero $g(y_*) = 0$. At any such zero, the leading negative terms of the series for $g(y)$ exactly cancel the trailing positive terms. From $g'(y) = y^{-1} \sum_n 2n(2-b_n)y^{2n}$, we find that $g'(y_*) > (2N/y_*)g(y_*) = 0$. So $g(y)$ can only change sign from negative to positive, and cannot return to 0 as $g'(y_*) \leq 0$ at the next zero. We conclude that the zero y_* is unique. Setting $x_* = A^{-1/2}y_*$, we conclude that $f'(x) < 0$ for $x \in (0, x_*)$ and $f'(x) > 0$ for $x \in (x_*, \infty)$, as claimed.

References

- [1] B. Akers and W. Gao. Wilton ripples in weakly nonlinear model equations. *Commun. Math. Sci.*, 10(3):1015–1024, 2012.
- [2] T. B. Benjamin. Instability of periodic wavetrains in nonlinear dispersive systems. *Proc. Roy. Soc. (London) Ser. A*, 299:59–76, 1967.
- [3] T. B. Benjamin and J. E. Feir. The disintegration of wave trains on deep water. *J. Fluid Mech.*, 27:417–430, 1967.
- [4] P. Chossat and F. Dias. The 1: 2 resonance with $O(2)$ symmetry and its applications in hydrodynamics. *Journal of Nonlinear Science*, 5(2):105–129, 1995.
- [5] W. Craig and C. Sulem. Numerical simulation of gravity waves. *Journal of Computational Physics*, 108(1):73–83, 1993.

- [6] C. W. Curtis and B. Deconinck. On the convergence of Hill’s method. *Maths. of Computation*, 79:169–187, 2010.
- [7] B. Deconinck and J. N. Kutz. Computing spectra of linear operators using the Floquet-Fourier-Hill method. *Journal of Comp. Physics*, 219:296–321, 2006.
- [8] B. Deconinck and K. Oliveras. The instability of periodic surface gravity waves. *J. Fluid Mech.*, 675:141–167, 2011.
- [9] B. Deconinck and O. Trichtchenko. Stability of periodic gravity waves in the presence of surface tension. *Eur. J. Mech. B Fluids*, 46, 2014.
- [10] C.V. Easwaran and S.R. Majumdar. Instability of capillary-gravity waves in water of arbitrary uniform depth. *Wave motion*, 9(6):483–492, 1987.
- [11] S. E. Haupt and J. P. Boyd. Modeling nonlinear resonance: a modification to the Stokes’ perturbation expansion. *Wave Motion*, 10(1):83–98, 1988.
- [12] D. M. Henderson and J. L. Hammack. Experiments on ripple instabilities. part 1. resonant triads. *J. Fluid Mech*, 184:15–41, 1987.
- [13] P. D. Hislop and I. M. Sigal. *Introduction to spectral theory*, volume 113 of *Applied Mathematical Sciences*. Springer-Verlag, New York, 1996. With applications to Schrödinger operators.
- [14] M. A Johnson and K. Zumbrun. Convergence of Hill’s method for nonselfadjoint operators. *SIAM Journal on Numerical Analysis*, 50(1):64–78, 2012.
- [15] M.C.W. Jones. Nonlinear stability of resonant capillary-gravity waves. *Wave Motion*, 15:267–283, 1992.
- [16] M.C.W. Jones. Evolution equations and stability results for finite-depth Wilton ripples. *International Journal of Non-Linear Mechanics*, 31:41–57, 1996.
- [17] T. Kawahara. Oscillatory solitary waves in dispersive media. *J. Phys. Soc. Jpn.*, 33:1015–1024, 1972.
- [18] M. S. Longuet-Higgins. The instabilities of gravity waves of finite amplitude in deep water. I. Superharmonics. *Proc. Roy. Soc. London Ser. A*, 360:471–488, 1978.
- [19] M. S. Longuet-Higgins. The instabilities of gravity waves of finite amplitude in deep water. II. Subharmonics. *Proc. Roy. Soc. London Ser. A*, 360:489–505, 1978.
- [20] R. S. MacKay and P.G. Saffman. Stability of water waves. *Proc. R. Soc. London A*, 406:115–125, 1986.
- [21] L. F. McGoldrick. An experiment on second-order capillary gravity resonant wave interactions. *Journal of Fluid Mechanics*, 40:251–271, 1970.
- [22] L. F. McGoldrick. On Wilton’s ripples: a special case of resonant interactions. *Journal of Fluid Mechanics*, 42:193–200, 1970.
- [23] L. F. McGoldrick. On the rippling of small waves: a harmonic nonlinear nearly resonant interaction. *Journal of Fluid Mechanics*, 52:725–751, 1971.
- [24] J. W. McLean. Instabilities of finite-amplitude water waves. *J. Fluid Mech.*, 114:315–330, 1982.
- [25] J. A. Sethian and J. Wilkening. A numerical model of stress driven grain boundary diffusion. *J. Comput. Phys.*, 193(1):275–305, 2004.
- [26] G. G. Stokes. On the theory of oscillatory waves. *Mathematical and Physical Papers*, 1:197–229, 1847.

- [27] O. Trichtchenko, B. Deconinck, and J. Wilkening. The instabilities of near-resonant and resonant periodic travelling gravity waves in the presence of surface tension. *In preparation*, 2016.
- [28] J.-M. Vanden-Broeck. *Gravity-Capillary Free-Surface Flows*. Cambridge University Press, Cambridge, 2010.
- [29] V. Vasan and B. Deconinck. The Bernoulli boundary condition for traveling water waves. *Appl. Math. Lett.*, 26(4):515–519, 2013.
- [30] G. B. Whitham. Non-linear dispersion of water waves. *J. Fluid Mech.*, 27:399–412, 1967.
- [31] S. Wiggins. *Introduction to applied nonlinear dynamical systems and chaos*. Springer, 1990.
- [32] J. Wilkening and J. Yu. Overdetermined shooting methods for computing standing water waves with spectral accuracy. *Computational Science & Discovery*, 5(1):014017, 2012.
- [33] J.R. Wilton. On ripples. *Philosophical Magazine Series 6*, 29(173):688–700, 1915.
- [34] V. E. Zakharov. Stability of periodic waves of finite amplitude on the surface of a deep fluid. *J. Appl. Mech. Tech. Phys.*, 9:190–194, 1968.